Korean J. Chem. Eng., 39(8), 2229-2238 (2022)
DOI: 10.1007/s11814-022-1092-5

pISSN: 0256-1115
eISSN: 1975-7220

A novel recyclable nano-adsorbent for enhanced oil recovery with efficient removal of Ca^{2+} and Cr^{6+} from oilfield wastewater

Lei He*,‡, Yong Dai*,‡, Zhe Wang, Lutao Yang*, Luxia Zhang*, Pengpeng Hu*, Yu Tian*, Hong Mo*, Haomiao Zhu*,†, and Jun Zhang*,†**

*Jiangsu Collaborative Innovation Center of Biomedical Functional Materials, National and Local Joint Engineering Research Center of Biomedical Functional Materials, Jiangsu Engineering Research Center of Biomedical Function Materials, School of Chemistry and Materials Science, Nanjing Normal University, Nanjing 210023, China
**Key Laboratory of Oilfield Chemistry, Research Institute of Petroleum Exploration and Development (RIPED), CNPC, Beijing 100083, China
(*Received 25 March 2021 • Revised 18 January 2022 • Accepted 20 February 2022*)

Abstract−Oilfield wastewater has a significantly negative influence on the recovery efficiency due to its hypersalinity. Therefore, magnetic graphene oxide (GO) modified with ethylene diamine tetraacetic acid (EDTA) and grafted by polyethylene glycol (PEG) nano-adsorbent was prepared to remove the Ca^{2+} and Cr^{6+} in Jidong Oilfield wastewater specifically. It was noteworthy that PEG-*g*-EDTA/Fe_3O_4/GO nano-adsorbent had excellent adsorption performance, with removal ratios up to 71.6% for Ca^{2+} and 42.7% for Cr^{6+} at 30 min. After the fifth recycling run, the nano-adsorbent still remained with high removal ratios (69.3% for Ca^{2+} and 30.5% for Cr^{6+}) and high reuse rates (89.4% for Ca^{2+} and 95.2% for Cr^{6+}), indicating that the nano-adsorbent had outstanding adsorption-desorption efficacy and high reusability. The adsorption test results demonstrated that the total salinity of the treated oilfield wastewater decreased by about 5,000 ppm, and the displacement efficiency further increased by 12.5% by chemical flooding compared with the untreated wastewater. Therefore, PEG-*g*-EDTA/Fe_3O_4/GO nano-adsorbent is an adsorbent with excellent potential which can effectively remove Ca^{2+} and Cr^{6+} in oilfield wastewater to enhance oil recovery (EOR).

Keywords: Oilfield Wastewater, Hypersalinity, Graphene Oxide, Adsorbent, Reusability, Enhance Oil Recovery

INTRODUCTION

Oil exploitation usually generates large amount of hypersaline wastewater [1-3]. Improper treatment of oilfield wastewater causes serious environmental pollution that is harmful to human health [4,5]. Wastewater reinjection into oilfield provides an optional way to enhance oil recovery and to alleviate the pollution problem [6-9], but the recovery efficiency is still affected by the high concentration of ions, which hinders the emulsifying process of oil. Removing metal ions from the oilfield wastewater is of vital importance.

Efficient adsorption has been recognized as one of the most promising methods in removing the metal ions [10,11]. The Fenton reaction has been reported as a feasible way to enhance the removal effect of Cr(VI) from water [12]. Graphene oxide (GO) is an excellent base material for adsorbent to rapidly remove the metal ions due to its high surface area-to-volume ratio and superior adsorption potential [13-15]. Sun et al. prepared Fe_3O_4/TiO_2/graphene (FTG) adsorbent to remove the Cu^{2+} from wastewater, with a maximal adsorption capacity of 87.4 mg/g [16]. Sheikhmohammadi et al. prepared magnetic graphene oxide (GO-Fe_3O_4) functionalized with 2-mercaptobenzothiazole (MBT) chelating ligand and used it to adsorb of Cr(VI) from aqueous solutions. The adsorption capacity was measured 4.41 mg/L [17]. Bafrooee et al. functionalized magnetic GO with ethylenediamine (EDA) and achieved an adsorption capacity of 13.3 mg/g for As(III) [18].

However, the application of GO is limited by inherent defects, making it difficult to reproduce and preserve [19]. Promoting the dispersity of GO in water is a feasible method to maximize the application. You et al. improved the dispersion and stability of GO in water by the non-covalent π-π interaction between graphene and tryptophan [20]. Liu et al. prepared montmorillonite (MMT) column-supported GO, effectively preventing GO aggregation, thus keeping a high surface area and adsorption performance [21]. Additionally, the magnetization modification of GO can effectively promote the adsorbent's recoverability through a magnetic field [22, 23]. Sheikhmohammadi et al. synthesized 8-hydroxyquinoline-functionalized GO-Fe_3O_4 nanocomposite (8-HQ-GO-Fe_3O_4) to remove Cr(VI) from aqueous solution. The maximum adsorption capacity was predicted to be 11.9 mg/g by isotherm model and kinetics, which was in mechanism quasi-second-order kinetics model with intra particle diffusion [24]. Among current magnetic nanoparticles, Fe_3O_4 has high magnetic saturation strength, low toxicity, large specific surface area, simple and diverse preparation methods, but meanwhile suffers limited adsorption capacity and low efficiency. In practice Fe_3O_4 nanoparticle is often chemically modified to improve the adsorption efficiency and recovery performance.

Introducing appropriate polymers or small polar molecules is

†To whom correspondence should be addressed.
E-mail: nickzhm@163.com, zhangjun3@njnu.edu.cn
‡These authors contributed equally to this work.
Copyright by The Korean Institute of Chemical Engineers.

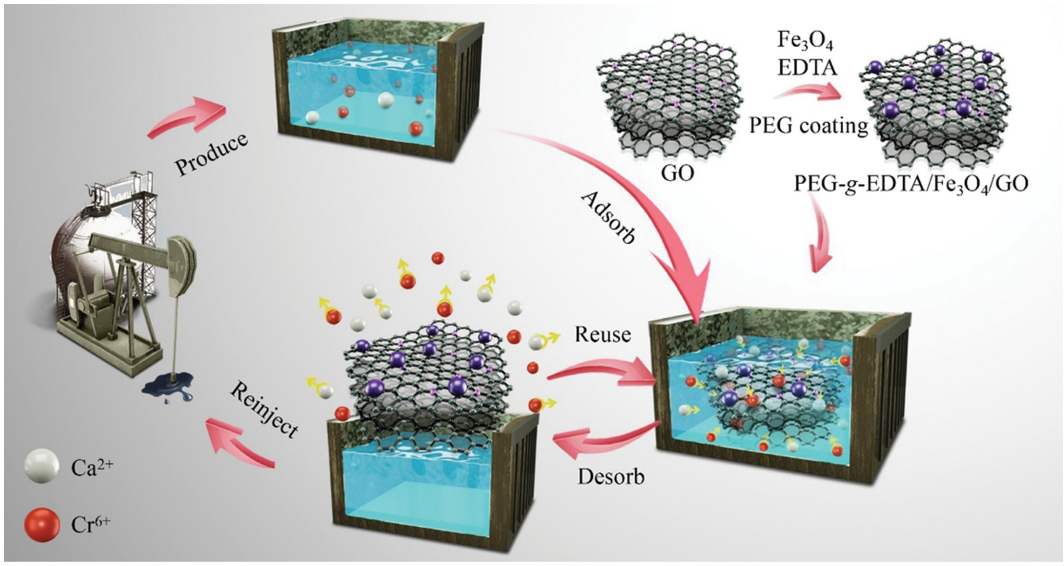


Fig. 1. Schematic diagram of preparation and application of PEG-*g*-EDTA/Fe_3O_4/GO.

superior to other substances to protect the lamellar structure of GO from being destroyed after magnetization modification, thus preserving adsorption capacity and prolonging life.

Rasoulzadeh et al. prepared chitosan-coated Fe_3O_4 particles for Pb(II) adsorption [25]. EDTA is also used for modification because of strong chelating performance [26]. Madadrang et al. modified GO with EDTA to remove the Pb^{2+} from water. The ultrahigh capacity of 479 mg/g for adsorbing Pb^{2+} at a pH of 6.8 indicated that the intercalation of EDTA greatly increased the adsorption capacity of GO [27]. PEG has been extensively applied because of its excellent water solubility and stability; there are several reports about the usage of PEG as a coating material to remove the metal ions from the oilfield wastewater [28]. Chan et al. covered Co-Fe_2O_3 with PEG onto polyether sulfone (PES) film, which significantly increased the removal ratio for Cu^{2+} [29]. Samadi et al. prepared PEG-modified Nd-TiO_2/GO nano-adsorbents for Pb^{2+} adsorption, and found that the dosage of adsorbent and adsorption time were reduced significantly after PEG modification at the same adsorption capacity [30].

In this work, EDTA and PEG were used for modification of magnetized GO to prepare PEG-g-EDTA/Fe_3O_4/GO nano-adsorbent (Fig. 1). The removal capacities of Ca^{2+} and Cr^{6+} were measured, the reusability was evaluated by recycling. In core displacement test, the improved recovery efficiency was revealed for oilfield wastewater treated by the novel nano-adsorbent.

MATERIALS AND METHODS

1. Materials

Graphene oxide, ferric trichloride hexahydrate ($FeCl_3 \cdot 6H_2O$, 99%) and ferrous sulfate heptahydrate ($FeSO_4 \cdot 7H_2O$, 99%) were purchased from Aladdin Biochemical Technology Co., Ltd. (Shanghai, China). Ethylenediamine tetraacetic acid (EDTA, 98%), N,N-dimethylformamide (DMF, 99.8%), 1-(3-Dimethylaminopropyl)-3-ethylcarbodiimide (EDC), 1,1-cyclohexanediacetic acid (CDA, 97%), methanol (CH_2OH, 99.9%), and sodium dodecyl sulfonate (SDS, 98%) were bought from Sinopharm Chemical Reagent Co., Ltd. (Nanjing, China). PEG-6000 was purchased from Baishun Biotechnology Co., Ltd. (Shanghai, China). The above reagents were analytically pure (AR).

2. Methods

2-1. Preparation of PEG-*g*-EDTA/Fe_3O_4/GO

GO was prepared by a new modified Hummers method [31]. The prepared GO (0.2 g) was put into deionized water (DI) (150 mL) to disperse evenly. $FeCl_2 \cdot 4H_2O$ (0.4 g) and $FeCl_3 \cdot 6H_2O$ (1.2 g) were ground in powder and put into the GO dispersion before 40-min sonication. Then the pH of the mixture was adjusted to 8.5 with $NH_3 \cdot H_2O$ (25 wt%) before 5-min sonication at 80 °C. The mixture was mechanically stirred (1,200 rpm) at 50 °C for 2 h and cooled to room temperature. Magnetic GO (Fe_3O_4/GO) powder (purity of 98.1%) was obtained after centrifugation, washing and drying.

The prepared Fe_3O_4/GO (0.5 g) and EDTA (3.5 g) were dispersed into DMF (150 mL) before 40-min sonication. CDA (80 mL) and EDC (0.4 g) were added and the mixture was mechanically stirred (1,500 rpm) for 4.5 h at 60 °C. Then it was cooled to room temperature. The EDTA/Fe_3O_4/GO powder (purity of 98.6%) was obtained after centrifugation, washing and drying.

The prepared EDTA/Fe_3O_4/GO (0.5 g) was dispersed into CH_2OH (200 mL) before 20-min sonication. Then CDA (0.2 g) and PEG-6000 (0.4 g) were put into the mixture before 30-min sonication using an ultrasonic cell morcellator. The mixture was mechanically stirred (1,800 rpm) for 4 h at 80 °C. Then it was cooled to room temperature. The PEG-*g*-EDTA/Fe_3O_4/GO powder (purity of 98.8%) was obtained after centrifugation, washing and drying.

2-2. Characterizations

Transmission electron microscope (TEM): Each sample (50 mg) was dispersed into DI (200 mL) to create a suspension. The suspension was spread on a copper grid after 20 min of sonication. The sample was allowed to stand until dry and tested with a Jeol

2100F TEM instrument (Japan).

X-Ray diffraction (XRD): Each sample was tested with Ultima IV X-ray diffractometer (Germany). Instrumental parameters included the following: a Cu target as the radiation source, test voltage of 40 kV, test current of 40 mA, 2θ of 5-90°, and scanning rate of 5°/min.

2-3. Adsorption Tests

This work aimed to treat Jidong Oilfield wastewater; thus, in the following experiments, we simulated the contents of Ca^{2+} and Cr^{6+} and the pH (7.2) and reservoir temperature (60 °C) in Jidong Oilfield wastewater.

The adsorption test for Ca^{2+} was performed using a titration method. The concentration of Ca^{2+} in the Jidong Oilfield wastewater is approximately 2.378×10^3 mg/L. Anhydrous $CaCl_2$ and DI were used to prepare calcium solution (Ca^{2+} concentration: c_a=2,252.0 mg/L). $NH_3\cdot H_2O$-$(NH_4)_2SO_4$ buffer solution (20 mL, pH=10) and the prepared calcium solution (20 mL) were added into a conical flask. Then the acquired solution was titrated using EDTA solution (with eriochrome black T as the indicator) until the solution turned pure blue. C_b is the concentration of Ca^{2+} remaining after adsorption. V_a and V_b are the volumes of EDTA solution consumed before and after adsorption, respectively.

After the adsorption for Ca^{2+}, the equation of removal rate (R_1) for Ca^{2+} was as follows:

$$R_1=\frac{C_a-C_b}{C_a}=1-\frac{V_a}{V_b} \quad (1)$$

Removal rates for Ca^{2+} were calculated at 10, 15, 20, 25, 30, 45, 60 and 120 min, respectively.

The Cr^{6+} concentration in the Jidong Oilfield wastewater was about 50.36 mg/L. $K_2Cr_2O_7$ (50 mg) was dissolved in DI (400 mL) (Cr^{6+} concentration: 44.2 mg/L). Then PEG-*g*-EDTA/Fe_3O_4/GO nano-adsorbent was added in and the thermostatic oscillator was to vibrate the mixed solution. At 10, 15, 20, 25, 30, 45, 60 and 120 min, supernatant (1.5 mL) was taken to measure the absorbance and the concentration of Cr^{6+} can be calculated based on the standard curve (Fig. S1).

An adsorption test for Cr^{6+} was performed with a spectrophotometer and DPCI color rendering method. $K_2Cr_2O_7$ was used as the active ingredient to prepare 10 g/L stock solution and 5 mg/L standard solution. 0 mL, 1 mL, 2 mL, 3 mL, 4 mL, 5 mL, 6 mL, 7 mL, 8 mL, 9 mL and 10 mL of 5 mg/L Cr^{6+} standard solution was put into flasks, respectively. The H_3PO_4 (0.5 mL, 50 v%), H_2SO_4 (0.5 mL, 50 v%) buffer solution and DPCI solution (2 mL) were added into the above flasks and diluted to a constant volume of 50 mL, respectively. The mixed solutions needed to stand still for 5 min for colorizing of Cr^{6+}. Then spectrophotometer was used to test absorbance at the site with a wavelength at 540 nm.

2-4. Recycling and Reusing Test

After the adsorption for Ca^{2+}, PEG-*g*-EDTA/Fe_3O_4/GO was collected by magnet.

Regeneration of PEG-*g*-EDTA/Fe_3O_4/GO was achieved by washing with 25 wt% $H_2C_2O_4$ solution (pH 2.0). The adsorption performance of PEG-*g*-EDTA/Fe_3O_4/GO was measured for five cycles. In the same way, NaOH was used to desorb and cycle experiment of Cr^{6+}.

The reuse rate (R_2) is calculated as the following equation:

$$R_2=\frac{m_b}{m_a}\times100\% \quad (2)$$

where m_b is the mass of the recycled PEG-*g*-EDTA/Fe_3O_4/GO and m_a is the initial mass of PEG-*g*-EDTA/Fe_3O_4/GO for adsorption. The experiment was repeated five times.

2-5. Laboratory Oil Displacement Experiment

Salinity test: PEG-*g*-EDTA/Fe_3O_4/GO (0.4 g) was put into Jidong Oilfield wastewater (400 mL). The mixed solution was stirred for 2 h to collect the supernatant. HNO_3 and $HClO_4$ (4 : 1) was used to remove the organic substances before testing. The contents of the metal ions were tested with PerkinElmer 8300 inductively coupled plasma optical emission spectrometer (Germany).

Interfacial tension test: The rotating droplet method is usually used to test the interfacial tension in the oilfield. Sodium dodecyl sulfonate (SDS) and the oilfield wastewater before and after the treatment of PEG-*g*-EDTA/Fe_3O_4/GO were prepared into a concentration of 0.3%, respectively. The interfacial tension was tested by KRUSS interface tensiometer (Germany). The crude oil from Jidong Oilfield was selected as target crude oil. The testing temperature was 60 °C and the speed was 5,000 r/min. Interfacial tension calculation is supported in information formulas S3, S4 and S5 (Supplementary information 11).

Displacement experiment: Berea cores are essential in displacement experiments. The test data of the Berea core are shown in Tables S4 and S5 (Supplementary information 13).

The displacement efficiency was measured according to the displacement experiment steps (Supplementary information 13).

Data analysis. Unless specified, each trial was triplicated. All data were expressed by mean±standard deviation (SD). Analysis of variance (ANOVA) was used for statistical comparation, followed by Bonferroni as post hoc test to determine the statistical significance between two groups; $p<0.05$ was considered as statistically significant.

RESULTS

1. Characterization

The TEM images of GO, Fe_3O_4/GO, EDTA/Fe_3O_4/GO, PEG-*g*-EDTA/Fe_3O_4/GO and HRTEM images of EDTA/Fe_3O_4/GO, PEG-*g*-EDTA/Fe_3O_4/GO are shown in Fig. 2. Fig. 2A shows that GO had a clear, thin and lamellar structure. As Fig. 2B shows, there were homogeneous black nanoparticles in the interlayer space, indicating that Fe_3O_4 nanoparticles had successfully bound to GO. As for Fig. 2C, there was an obvious lamellar overlay structure of the folds at the margins of EDTA/Fe_3O_4/GO. Fig. 2E is the HRTEM image of EDTA/Fe_3O_4/GO, Fe_3O_4 nanoparticles had a diameter of about 9 nm and a single lattice thickness of 3.4 Å. Fig. 2D is the TEM image of PEG-*g*-EDTA/Fe_3O_4/GO, the lamellated structure accompanied by small Fe_3O_4 nanoparticles on each surface. But the nanoparticles were vague and seemingly covered by transparent enveloped coat. Fig. 2F is the HRTEM image of PEG-*g*-EDTA/Fe_3O_4/GO; it was fuzzier compared with the HRTEM image of EDTA/Fe_3O_4/GO (Fig. 2E). The diameter of Fe_3O_4 nanoparticles was about 8 nm, surrounded by a relatively fuzzy layer, namely PEG. It indicated that PEG had successfully modified the surface of EDTA/

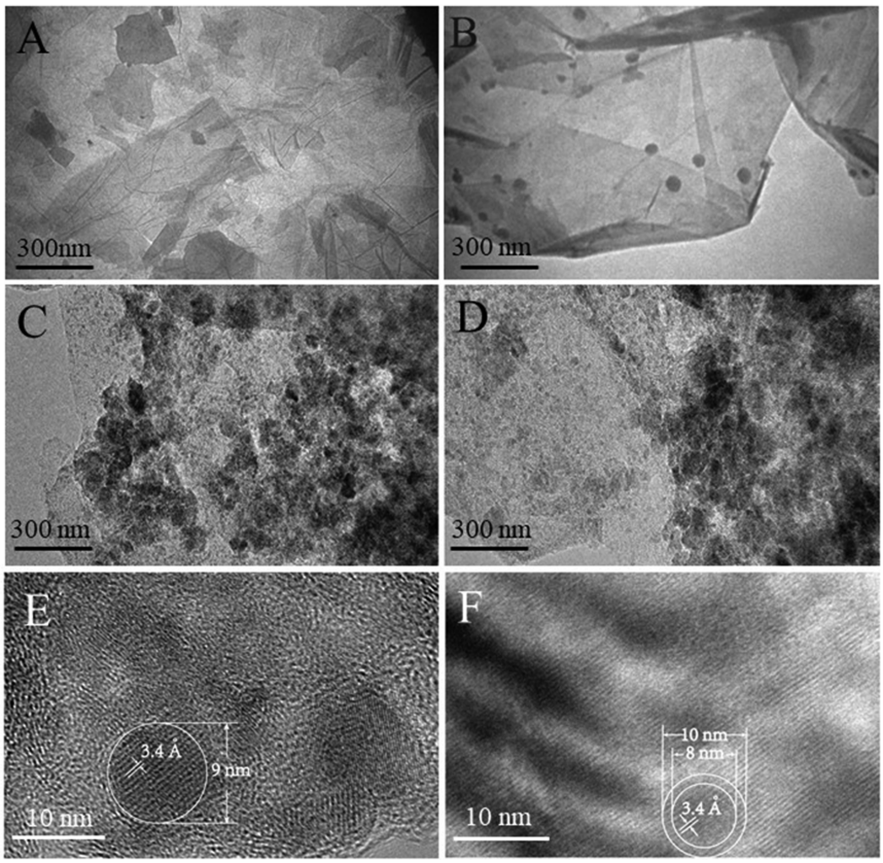


Fig. 2. TEM images of (A) GO, (B) Fe_3O_4/GO, (C) EDTA/Fe_3O_4/GO and (D) PEG-*g*-EDTA/Fe_3O_4/GO, HRTEM images of (E) EDTA/Fe_3O_4/GO and (F) PEG-*g*-EDTA/Fe_3O_4/GO.

Fe_3O_4/GO. The results of TEM characterization correspond to the representation and shape of AFM (Fig. S2) and SEM (Fig. S3).

AFM images of GO, Fe_3O_4/GO, EDTA/Fe_3O_4/GO and PEG-*g*-EDTA/Fe_3O_4/GO are shown in Fig. S1. Fig. S2A shows a clear lamellar structure of GO. The monolayer thickness was about 1.0 nm. Prominent raised Fe_3O_4 nanoparticles between the layers of GO can be seen in the Fig. S2B, and the nanoparticles grew between layers of GO [32]. The thickness of single layer was about 1.05 nm. As for Fig. S2C, EDTA/Fe_3O_4/GO had the same lamellae structure as GO and Fe_3O_4/GO, and the thickness of single lamellae was about 1.17 nm. The difference was in the folded lamellae superposition structure at the edge. Fig. S2D is the AFM image of PEG-*g*-EDTA/Fe_3O_4/GO, the nanoparticles on surface were relatively round and the thickness of the monolithic layer was improved slightly. Because Fe_3O_4 nanoparticles were coated with PEG after modification. The results are consistent with TEM characterization (Fig. 2).

SEM images of GO, Fe_3O_4/GO, EDTA/Fe_3O_4/GO and PEG-*g*-EDTA/Fe_3O_4/GO can be seen in Fig. S3. Fig. S3A shows that GO had coarse surface and lamellar thin-film structure. Fig. S3B shows that the surface of Fe_3O_4/GO was rougher than GO because of the intercalation of Fe_3O_4 nanoparticles. According to TEM characterization results, the diameter of the introduced magnetic nanoparticles was about 8 nm (Fig. 2E and F). As can be seen in Fig. S3C, EDTA/Fe_3O_4/GO had an irregular laminated structure and formed debris particles on the adsorption surface after modification with EDTA. In Fig. S3D, PEG-*g*-EDTA/Fe_3O_4/GO seem to have a thin film on its surface after further modification with PEG, so the Fe_3O_4

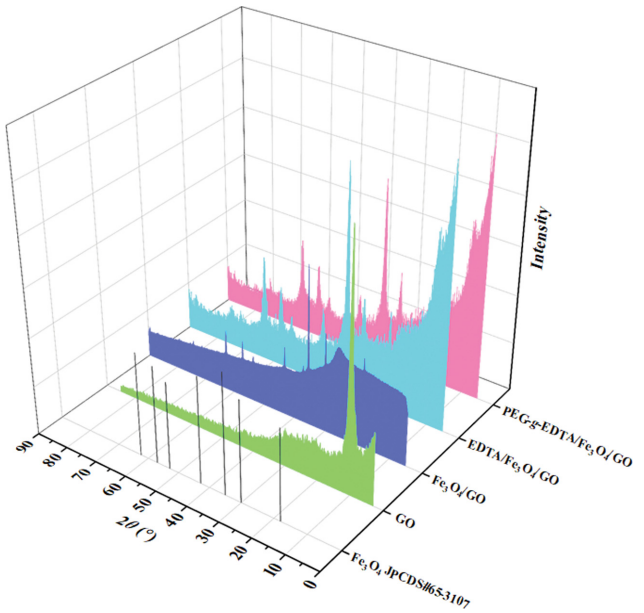


Fig. 3. XRD images of GO, Fe_3O_4/GO, EDTA/Fe_3O_4/GO and PEG-*g*-EDTA/Fe_3O_4/GO.

nanoparticles are enveloped with PEG. It was verified that PEG had successfully modified the surface of EDTA/Fe_3O_4/GO, which is consistent with TEM (Fig. 2) and AFM (Fig. S2) results.

The XRD images of GO, Fe_3O_4/GO, EDTA/Fe_3O_4/GO and PEG-*g*-EDTA/Fe_3O_4/GO are shown in Fig. 3. GO shows a characteristic peak at approximately 10.5°, meeting the crystal characteristics of GO [33]. Fe_3O_4/GO, EDTA/Fe_3O_4/GO and PEG-*g*-EDTA/Fe_3O_4/GO showed high coincidence with the diffraction angles of the standard card JPCDS#65-3107 because of Fe_3O_4 nanoparticles. The higher the oxidative degree, the smaller the angle of diffraction. Fe_3O_4/GO had an obviously broad peak at approximately 18°, because of the partial reduction of GO after modification, which led to reduction of oxidation degree and destruction of crystal pattern. EDTA/Fe_3O_4/GO also had an obviously dispersive broad peak at 15-25° because of the intercalation the Fe_3O_4 nanoparticles. However, PEG-*g*-EDTA/Fe_3O_4/GO shows an obvious peak at about 22°. The characteristic peaks shifted left slightly is due to the oxidation degree increased after the modification with PEG.

Fig. S4 is the FT-IR characterization. GO shows obvious characteristic peaks at 3,335 cm^{-1} (-OH stretch vibration), 1,734 cm^{-1} (-COOH stretch vibration) and 1,049 cm^{-1} (C-O-C stretch vibration), respectively. Compared to GO, the peak at 588 cm^{-1} (Fe-O stretch vibra-

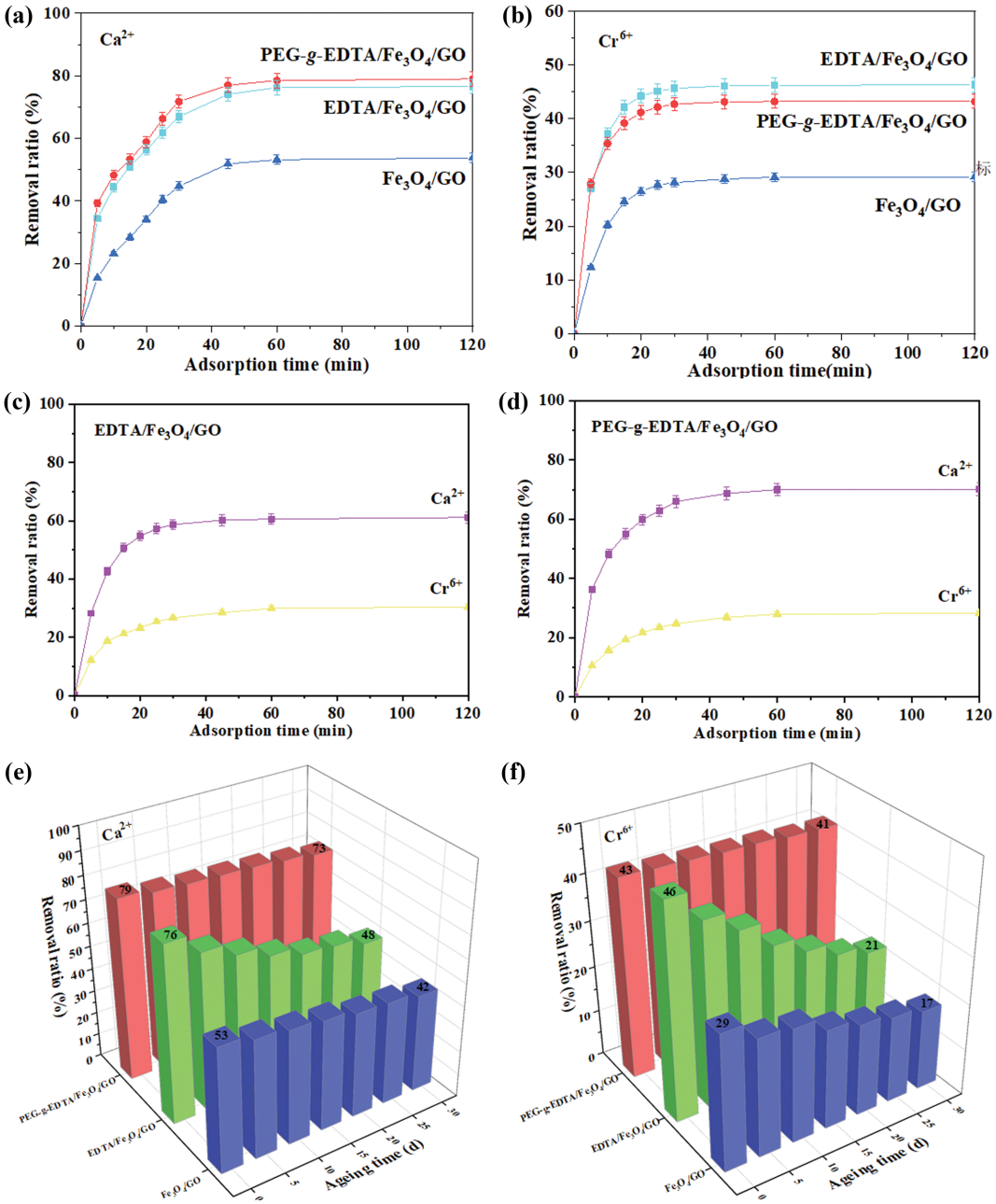


Fig. 4. Removal ratio of Fe_3O_4/GO, EDTA/Fe_3O_4/GO and PEG-*g*-EDTA/Fe_3O_4/GO for Ca^{2+} (a) and Cr^{6+} (b) at different adsorption times; co-adsorption removal ratios of EDTA/Fe_3O_4/GO (c) and PEG-*g*-EDTA/Fe_3O_4/GO (d) for both Ca^{2+} and Cr^{6+}; removal ratios of Fe_3O_4/GO, EDTA/Fe_3O_4/GO and PEG-*g*-EDTA/Fe_3O_4/GO for Ca^{2+} (e) and Cr^{6+} (f) at different ageing times.

tion), indicating that Fe_3O_4 nanoparticles had been successfully intercalated. EDTA/Fe_3O_4/GO showed obvious peaks at 1,401 cm^{-1} (C-N stretch vibration) and 588 cm^{-1} (Fe-O stretch vibration) because of magnetization and EDTA modification, respectively [34]. Compared with GO and Fe_3O_4/GO, the transmittance of EDTA/Fe_3O_4/GO and PEG-*g*-EDTA/Fe_3O_4/GO at the peak of 3,443 cm^{-1} was slightly reduced because of partial amidation of carboxyl. The peaks of PEG-*g*-EDTA/Fe_3O_4/GO at 2,925 cm^{-1} (-CH_2- stretch vibration) and 1,294 cm^{-1} (-O- stretch vibration) were caused by the modification of PEG [35].

The Raman image is shown in Fig. S4. All samples clearly show two characteristic peaks at 1,581 cm^{-1} and 1,332 cm^{-1}, which correspond to the D peak and G peak of the carbon ring in the graphene material. D peak is a reflection of crystal structure disorder and G peak characterizes the sp^2 bond structure of carbon. The intensity ratios (I_D : I_G) of the D peak and the G peak of GO and Fe_3O_4/GO were 0.86 and 2.19, respectively. The reason is that hexagonal structure of GO was destroyed after magnetization. The intensity ratios (I_D : I_G) of EDTA/Fe_3O_4/GO and PEG-*g*-EDTA/Fe_3O_4/GO were 1.23 and 1.34, which were slightly higher than GO but lower than Fe_3O_4/GO. It was because magnetization destroyed the GO hexagonal structures, resulting in a decrease in the value of D peak. During the process of PEG modification, CO-H bonds were introduced and resulted in the increase of oxygen content and the decrease of lamellar thickness, which led to a decrease in the peak value of G band compared with Fe_3O_4/GO [36].

2. Adsorption Tests of Ca^{2+} and Cr^{6+}

Fig. 4 shows the removal ratios of Ca^{2+} and Cr^{6+} by Fe_3O_4/GO, EDTA/Fe_3O_4/GO and PEG-*g*-EDTA/Fe_3O_4/GO according to different conditions. The removal ratios of Fe_3O_4/GO, EDTA/Fe_3O_4/GO and PEG-*g*-EDTA/Fe_3O_4/GO for Ca^{2+} were measured 53.8%, 76.6% and 79.0% at 120 min, respectively (Fig. 4(a)). The removal ratios of PEG-*g*-EDTA/Fe_3O_4/GO for Ca^{2+} were significantly higher than those of Fe_3O_4/GO and EDTA/Fe_3O_4/GO. Fig. 4(b) shows that the removal ratios of Fe_3O_4/GO, EDTA/Fe_3O_4/GO and PEG-*g*-EDTA/Fe_3O_4/GO for Cr^{6+} were measured 29.2%, 46.3% and 43.2% at 120 min, respectively. The removal ratios of PEG-*g*-EDTA/Fe_3O_4/GO for Ca^{2+} were significantly higher than those of Fe_3O_4/GO but slightly lower than EDTA/Fe_3O_4/GO. The removal ratios of PEG-*g*-EDTA/Fe_3O_4/GO for Ca^{2+} were measured 39.3%, 53.4% and 71.8% at 5, 15, 30 min, for Cr^{6+} were measured 27.9%, 39.2% and 42.7% at 5, 15, 30 min, respectively. It indicated that PEG-*g*-EDTA/Fe_3O_4/GO had high adsorption efficiency for Ca^{2+} and Cr^{6+}. Fig. 4(c) and (d) are co-adsorption removal ratios of EDTA/Fe_3O_4/GO and PEG-*g*-EDTA/Fe_3O_4/GO for both Ca^{2+} and Cr^{6+}. It can be seen that the removal ratios of Ca^{2+} and Cr^{6+} decreased during co-adsorption compared with adsorption alone, but the removal efficiency was still considerably high. Fig. 4(e) and F are removal ratios of Fe_3O_4/GO, EDTA/Fe_3O_4/GO and PEG-*g*-EDTA/Fe_3O_4/GO for Ca^{2+} and Cr^{6+} at different ageing times. The removal ratios of PEG-*g*-EDTA/Fe_3O_4/GO for Ca^{2+} slightly decreased from 79.0% to 72.4% at 120 min, and for Cr^{6+} slightly decreased from 43.2% to 41.2% after 30 d of aging, respectively. The removal ratios of EDTA/Fe_3O_4/GO for Ca^{2+} rapidly decreased from 76.6% to 48.4%, and for Cr^{6+} rapidly decreased from 46.3% to 21.7%, respectively. The removal ratios of EDTA/Fe_3O_4/GO were slightly higher than PEG-g-EDTA/Fe_3O_4/GO for Cr^{6+}, because aging had great negative influence on EDTA/Fe_3O_4/GO. The results show that PEG-*g*-EDTA/Fe_3O_4/GO is much higher than EDTA/Fe_3O_4/GO in terms of comprehensive performance.

3. Adsorption Mechanism

PEG-*g*-EDTA/Fe_3O_4/GO simultaneously adsorbed Ca^{2+} and Cr^{6+} by both physical and chemical methods. Physical adsorption was one of the important processes of GO adsorption for Ca^{2+} and Cr^{6+}, because of rich pore structure. However, the effect of chemical adsorption was particularly prominent. Fig. 5 is the schematic diagram of the proposed chemical adsorption mechanism. The chemical adsorption was mainly driven by the coordination effect between the functional group (-COOH, -OH, -O-, -CO-H) of the adsorbent and metal ions. As shown in Fig. 5, one calcium ion could coordi-

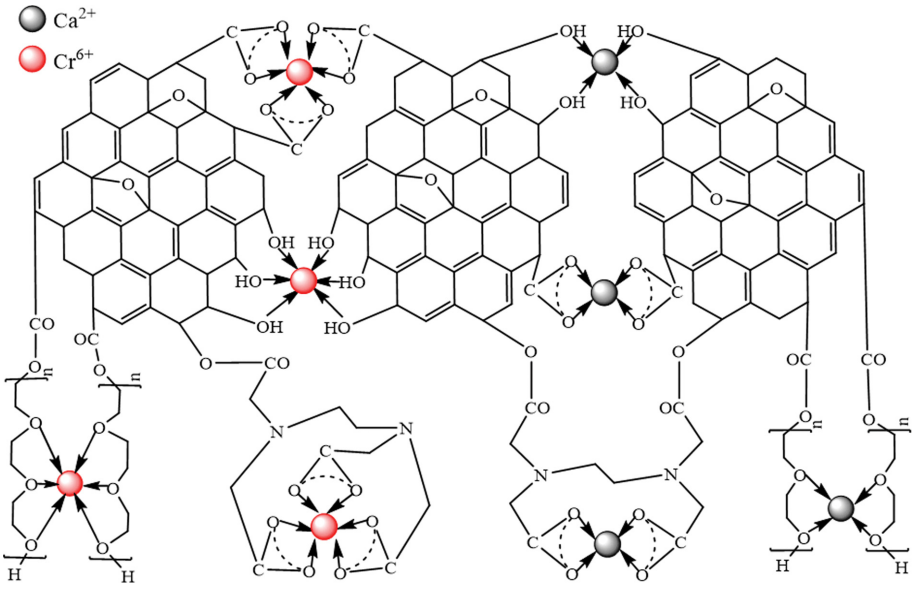


Fig. 5. Chemical adsorption mechanism diagram.

nate with four oxygen atoms (-OH, -COOH, -O- and -CO-H) while one chromium ion could coordinate with six. The increase of adsorption capacity was mainly due to the abundance of -OH and -COOH in EDTA and PEG, which resulted in more mating sites and could be illustrated in Fig. S6.

A wide scan of Ca^{2+} and Cr^{6+} adsorbed on PEG-*g*-EDTA/Fe_3O_4/GO is shown in Fig. S6(b). The Ca(2p), Cr(2p), Cl(2p) and K(2p) peak were observed at 346.6 eV, 574.3 eV, 198.7 eV and 294.1 eV, respectively. The high-resolution Ca(2p) peaks of Ca^{2+} adsorbed on PEG-*g*-EDTA/Fe_3O_4/GO are shown in Fig. S6(c). The peaks of Ca-O and Ca-Cl appeared at 346.9 eV and 350.6 eV indicated that the adsorption for Ca^{2+} was acting by both physical and chemical adsorption. The high-resolution Cr(2p) peaks of Cr^{6+} adsorbed on PEG-*g*-EDTA/Fe_3O_4/GO are shown in Fig. S6(d). The peaks of $Cr(2p_{1/2})^{6+}$-O, $Cr(2p_{1/2})^{3+}$-O, $Cr(2p_{3/2})^{6+}$-O and $Cr(2p_{3/2})^{3+}$-O were observed at 587.1 eV, 585.9 eV, 577.6 eV and 576.2 eV, respectively. It could be speculated that $K_2Cr_2O_7$ was adsorbed by both physical adsorption chemical adsorption.

4. Reuse of PEG-*g*-EDTA/Fe_3O_4/GO

PEG-*g*-EDTA/Fe_3O_4/GO was recycled for five times to assess reusability. The reuse rates and removal ratios of PEG-*g*-EDTA/Fe_3O_4/GO for Ca^{2+} are shown Fig. 6(a). At the fifth recycling run, the PEG-*g*-EDTA/Fe_3O_4/GO still reserved high reuse rates (89.4%) and removal ratios (69.3%). Fig. 6(b) shows the reuse rates and removal ratios of PEG-*g*-EDTA/Fe_3O_4/GO for Cr^{6+}. At the fifth recycling run, the PEG-*g*-EDTA/Fe_3O_4/GO still reserved relatively high reusability (95.2%) and removal rate (30.5%). It indicated that PEG-*g*-EDTA/Fe_3O_4/GO adsorbent had high reusability.

5. Laboratory Oil Displacement Experiment

Salinity test results: The concentrations of metal ions in the oilfield wastewater before and after treatment with PEG-*g*-EDTA/Fe_3O_4/GO are shown in Table 1. It can be seen that the Ca^{2+} content decreased from 2,435 mg/L to 742 mg/L (decreased by 1,693 mg/L) and Cr^{6+} content decreased from 45 mg/L to 28 mg/L (decreased by 17 mg/L), with the total salinity decreased by 5,000 ppm.

Table 1. Concentrations and salinities of calcium and magnesium in oilfield stratum water and treated water

Elements	Oilfield water (mg/L)	Treated water (mg/L)
Calcium	2,435.31	742.25
Chromium	45.68	28.06
Sodium	6,386.5	6,136.9
Copper	0.08	0.06
Manganese	2.50	0.08
Strontium	4.53	2.35
Iron	1.15	1.05
Zinc	0.57	0.14
Nickel	0.04	0.02
Total salinity	23,000	18,000

The above results demonstrate that PEG-*g*-EDTA/Fe_3O_4/GO had good adsorbing effect for Ca^{2+} and Cr^{6+} in the oilfield wastewater.

Interfacial tension test: Fig. 7 shows the results of interfacial tension of the oilfield wastewater before and after being treated with PEG-*g*-EDTA/Fe_3O_4/GO. According to formulas S3, S4 and S5, the measured interfacial tension values of oilfield wastewater before and after being treated with PEG-*g*-EDTA/Fe_3O_4/GO were 2.5 N/m and 2.1×10^{-2} N/m, because of the strong destructive effect of Ca^{2+} and Cr^{6+} on the interface activity of SDS surfactant. The interface tension of treated oilfield wastewater decreased by two orders of magnitude, which can fully meet the actual requirements of chemical flooding interface tension less than 0.1 N/m in field application of oilfield.

Displacement experiments: Fig. 8(a) shows the results of the displacement experiment using untreated oilfield wastewater. The recovery efficiency of crude oil was 48.1% after water-flooding. After chemical-flooding and post-water flooding, the recovery efficiency of crude oil increased to 50.3%. Therefore, the displacement fluid prepared by oilfield wastewater containing Ca^{2+} and Cr^{6+} had lim-

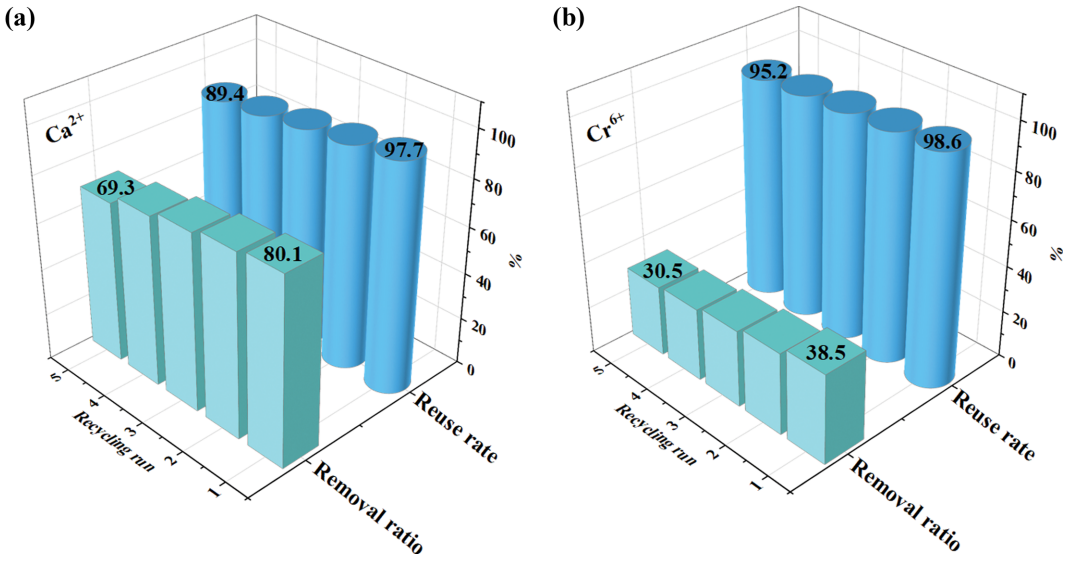


Fig. 6. The reusability of PEG-*g*-EDTA/Fe_3O_4/GO for Ca^{2+} (a) and Cr^{6+} (b).

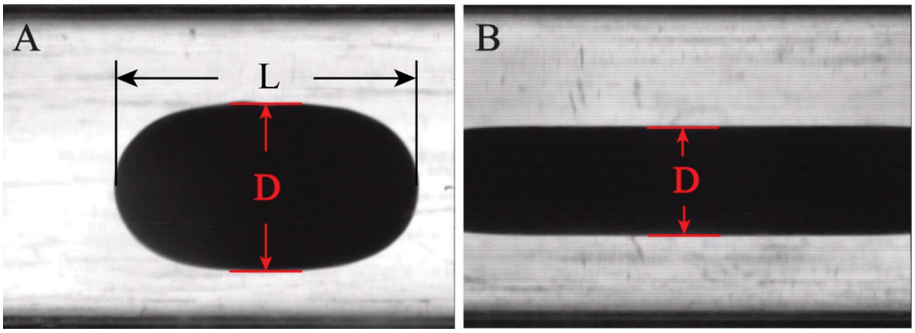


Fig. 7. Interfacial tension test of displacement fluid prepared by oilfield wastewater before (A) and after (B) treatment with PEG-*g*-EDTA/Fe_3O_4/GO.

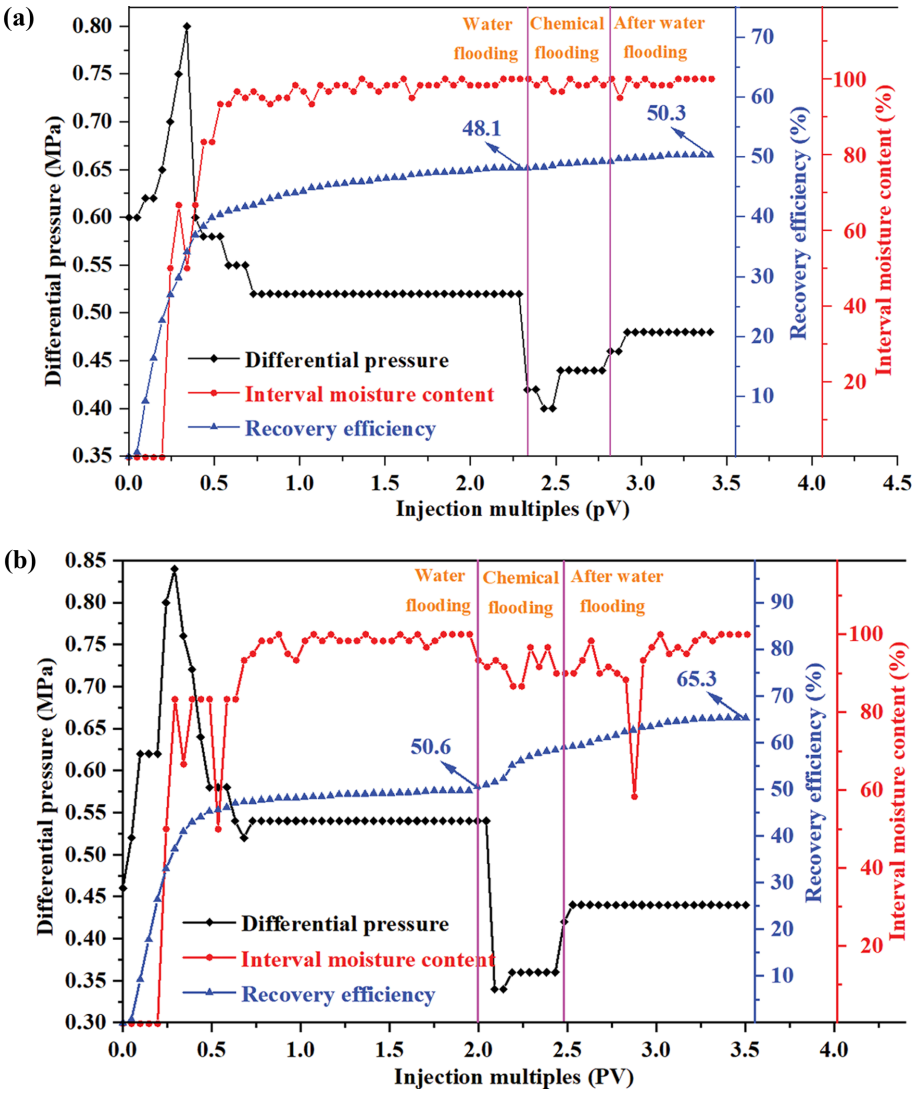


Fig. 8. Core displacement test in untreated oilfield wastewater (a) and (b).

ited function in EOR. It had increased the EOR of crude oil by only 2.2% relative to water-flooding. Fig. 8(b) shows the results of displacement experiments using oilfield wastewater treated with PEG-g-EDTA/Fe_3O_4/GO. The recovery efficiency was 50.6% after water-flooding. But the recovery efficiency of crude oil increased to 65.3% after chemical-flooding and post-water flooding. Relative to water-flooding, the EOR of crude oil increased by 14.7%. Compared with untreated oilfield wastewater, the treated oilfield wastewater (as the oil-displacing solution) significantly enhanced oil recovery (by 12.5%), indicating that PEG-*g*-EDTA/Fe_3O_4/GO

adsorbent had excellent potential in treating oilfield wastewater and enhanced oil recovery.

DISCUSSION

Oil is recognized as the "life blood" of industry. However, its exploitation has become increasingly difficult. Therefore, developing highly-efficient, environmentally-friendly and low-cost method is extremely urgent [37,38]. Oilfield wastewater needs to be reinjected to prevent pollution and save cost. However, a large amount of metal ions (Ca^{2+} and Cr^{6+}) in wastewater has a significant adverse effect to enhance oil recovery. In particular, sulfonate surfactants (e.g., sodium dodecyl sulfonate (SDS)) are the most affected, which substantially reduces oil recovery efficiency [39].

The wastewater of the Jidong Oilfield contained much more Ca^{2+} and Cr^{6+}. Because of the strong electrical neutralization of Ca^{2+} and the strong oxidation of Cr^{6+}, SDS will react with the ions. Then effectiveness was lost and recovery efficiency was reduced [40,41]. Therefore, if oilfield wastewater is reinjected as the recycling water without being treated, whose chemical reaction with oil-displacing agents may greatly reduce the recovery efficiency. So, it is necessary to remove Ca^{2+} and Cr^{6+} before reinjecting the oilfield wastewater.

Adsorption is one of the most effective methods for removing metal ions from water. According to the above experimental results, PEG-*g*-EDTA/Fe_3O_4/GO is an adsorbent with excellent performance. The removal ratio for Ca^{2+} at 5, 15, 30 min was 39.3%, 53.4% and 71.8%, for Cr^{6+} at 5, 15, 30 min was 27.9%, 39.2% and 42.7%, respectively (Fig. 4), which indicates high adsorption efficiency. The balance time for Ca^{2+} adsorption of PEG-*g*-EDTA/Fe_3O_4/GO is 60 min (Fig. 4(a)), and the balance time for Cr^{6+} adsorption is 40 min (Fig. 4(b)). The co-adsorption diagram shows that the optimum adsorption time was 60 min (Fig. 4(d)). Mopoung et al. modified waste carbon in pineapple leaf fiber with $KMnO_4$ to adsorb the Ca^{2+} from hard water, with a removal ratio for Ca^{2+} up to 78.7% and adsorption balance achieved at 60 min [42]. Chen et al. prepared the composite adsorbent of polyethyleneimine (PEI-GO) and GO to remove the Cr^{6+} from aqueous solution. The adsorption ratio for Cr^{6+} is 71% and adsorption balance time is 14 h [43]. Therefore, PEG-*g*-EDTA/Fe_3O_4/GO has a good performance in removing the Ca^{2+} and Cr^{6+} from oilfield wastewater.

Additionally, PEG-*g*-EDTA/Fe_3O_4/GO has prominent reusability. After the fifth recycling run, it still retained high recovery efficiency (89.4% for Ca^{2+} and 95.2% for Cr^{6+}) (Fig. 6). You et al. adopted sol-gel process in combination with Schiff base reaction to prepare benzo-crown ether functionalized silica, which was used to selectively adsorb Ca^{2+} with adsorption efficiency of 87-92% after the second recycling run [44]. Sun et al. synthetized N-doped hierarchical porous carbon (NHPC) extracted from silkworm cocoon and used the NHPC as a highly efficient adsorbent to remove the Cr^{6+} from wastewater, with 98% of initial adsorption performance retained after the fifth recycling run [45]. Although the reusability is slightly lower than that reported above, PEG-*g*-EDTA/Fe_3O_4/GO is still an excellent adsorbent in terms of overall adsorption efficiency and reusability.

In the oil field, metal ions are often used as crosslinking agent to improve plugging effect [46]. Therefore, Ca^{2+} and Cr^{6+} desorbed from PEG-*g*-EDTA/Fe_3O_4/GO can be continuously used as crosslinking agents after reduction. It not only improves efficiency and reduces costs, but also reduces pressure on the environment when metal ions are used for plugging.

Sulfonate surfactant is one of the commonly used surfactants in oil fields. However, the large number of metal ions in reinjection water limits its use, so it is often used to compound or modify. Liu et al. synthesized three types of alkyl alcohol polyoxyethylene ether sulfonates, and the recovery efficiency increased by 16.19-19.38% [47]. Pu et al. combined glucosamine sulfonate surfactant with the modified polyacrylamide to enhance oil recovery, and the recovery efficiency increased by 16.05% [48]. In this work, we only removed the Ca^{2+} and Cr^{6+} from oilfield wastewater to enhance oil recovery of SDS. The results show that recovery efficiency was significantly increased by 14.7% using only SDS and the treated oilfield wastewater. Therefore, PEG-*g*-EDTA/Fe_3O_4/GO is a promising adsorbent and removing Ca^{2+} and Cr^{6+} is an effective method to enhance oil recovery.

CONCLUSIONS

PEG-*g*-EDTA/Fe_3O_4/GO nano-adsorbent was prepared. This nano-adsorbent can effectively remove the Ca^{2+} and Cr^{6+} from oilfield wastewater and has high reusability. Relative to untreated oilfield wastewater, the oil recovery efficiency was significantly increased by 12.5% using the wastewater treated with PEG-*g*-EDTA/Fe_3O_4/GO. Therefore, PEG-*g*-EDTA/Fe_3O_4/GO nano-adsorbent has promising application prospect in treating oilfield wastewater and enhancing oil recovery.

ACKNOWLEDGEMENTS

The authors are grateful to the Nanjing Normal University, School of Chemistry and Materials Science, National and Local Joint Engineering Research Center of Biomedical Functional Materials, Jiangsu Engineering Research Center of Biomedical Function Materials, Key Laboratory of Oilfield Chemistry, Research Institute of Petroleum Exploration and Development (RIPED) for providing technical support.

DECLARATION OF COMPETING INTEREST

The authors have no competing financial interests to declare.

SUPPORTING INFORMATION

Additional information as noted in the text. This information is available via the Internet at http://www.springer.com/chemistry/journal/11814.

REFERENCES

1. H. Miller, K. Dias, H. Hare, M. Borton, J. Blotevogel, C. Danforth, J. A. Ippolito and T. Borch, *Sci. Total Environ.*, **722**, 137888 (2020).
2. Y. Q. Li, H. Zhang, C. Ma, H. Yin, L. Z. Gong, Y. S. Duh and R.

Feng, *Carbohydr. Polym.*, **226**, 115279 (2019).
3. H. Q. Chang, T. Li, B. C. Liu, R. D. Vidic, M. Elimelech and J. C. Crittenden, *Desalination*, **455**, 34 (2019).
4. Z. G. Wang, P. Y. Li, Y. Fang, L. Y. Yan, W. K. Zhou, X. M. Fan and H. Q. Liu, *Carbohydr. Polym.*, **223**, 115064 (2019).
5. J. E. Johnston, E. Lim and H. Roh, *Sci. Total Environ.*, **657**, 187 (2019).
6. J. H. Huang, L. X. Shi, G. M. Zeng, H. Li, H. Huang, Y. L. Gu, Y. H. Shi, K. X. Yi and X. Li, *J. Cleaner Prod.*, **209**, 53 (2019).
7. L. P. Fu, G. C. Zhang, J. J. Ge, K. L. Liao, H. H. Pei, P. Jiang and X. Q. Li, *Colloids Surf. A.*, **508**, 230 (2016).
8. J. X. Wang, L. Wang, C. Q. Xu, R. Zhi, R. Miao, T. Liang, X. L. Yue, Y. T. Lv and T. T. Liu, *Chem. Eng. J.*, **332**, 787 (2017).
9. Q. W. Chai, L. Lu, Y. Lin, X. Q. Ji, C. P. Yang, S. Y. He and D. Zhang, *Environ. Sci. Pollut. Res.*, **25**, 18443 (2018).
10. M. Hua, S. J. Zhang, B. C. Pan, W. M. Zhang, L. Lv and Q. X. Zhang, *J. Hazard. Mater.*, **211**, 317 (2012).
11. M. Ince and O. K. Ince, *Int. J. Pure Appl. Sci.*, **3**, 10 (2017).
12. A. Yazdanbakhsh, A. Aliyari, A. Sheikhmohammadi and E. Aghayani, *J. Water Process Eng.*, **34**, 101080 (2020).
13. V. D. Gohel, A. Rajput, S. Gahlot and V. Kulshrestha, *Macromol. Symp.*, **376**, 1700050 (2017).
14. F. E. Peer, N. Bahramifar and H. Younesi, *J. Taiwan Inst. Chem. Eng.*, **87**, 225 (2018).
15. Z. H. Dong, F. Zhang, D. Wang, X. Liu and J. Jin, *J. Solid State Chem.*, **224**, 88 (2015).
16. Y. H. Sun, S. Lv, C. D. Si, G. J. Liu and H. T. Gao, *J. Nanosci. Nanotechnol.*, **17**, 5400 (2017).
17. A. Sheikhmohammadi, S. M. Mohseni, B. Hashemzadeh, E. Asgari and M. Almasiane, *Desalin. Water Treat.*, **160**, 297 (2019).
18. A. A. T. Bafrooee, E. Moniri, H. A. Panahi, M. Miralinaghi and A. H. Hasani, *Res. Chem. Intermed.*, **47**, 1397 (2021).
19. X. L. Niu, Z. R. Wen, X. Y. Li, L. J. Yan, W. L. Zhang, S. X. Gong, Z. F. Shi and W. Sun, *Curr. Anal. Chem.*, **13**, 410 (2017).
20. F. You, D. R. Wang, X. X. Li, M. J. Liu, G. H. Hu and Z. M. Dang, *RSC Adv.*, **4**, 8799 (2014).
21. L. Liu, Y. R. Zhang, Y. J. He, Y. F. Xie, L. H. Huang, S. Z. Tan and X. Cai, *RSC Adv.*, **5**, 3965 (2014).
22. K. Gul, S. Sohni, M. Waqar, F. Ahmad, N. A. N. Norulaini and A. K. M. Omar, *Carbohydr. Polym.*, **152**, 520 (2016).
23. A. Kilic, E. Gezer, F. Durap, M. Aydemir and A. Baysal, *J. Organomet. Chem.*, **896**, 129 (2019).
24. A. Sheikhmohammadi, S. M. Mohseni, R. Khodadadi, M. Sardar, M. Abtahi, S. Mahdavi, H. Keramati, Z. Dahaghin, S. Rezaei and M. Almasian, *J. Mol. Liq.*, **233**, 75 (2017).
25. D. Hr, C. Mhdab, E. Asm, F. Rrk, B. Rn, B. Sn, G. Khk and I. Jnsh, *J. Mol. Liq.*, **297**, 111893 (2020).
26. J. L. Yun and S. Iqbal, *Micropor. Mesopor. Mater.*, **248**, 149 (2017).
27. C. J. Madadrang, H. Y. Kim, G. H. Gao, N. Wang, J. Zhu and H. Feng, *ACS Appl. Mater. Interfaces*, **4**, 1186 (2012).
28. E. J. Smolders, N. Thammajaruk, C. T. M. M. de Kanter, Y. Colbers, P. Chaiyahong, T. Cuprasitrut, S. Chittmittraprap, T. Apornpong, S. Khemnark, P. Tangkijvanich and D. M. Burger, A. *Trop. Med. Int. Health*, **23**, 295 (2018).
29. K. H. Chan, E. T. Wong, M. Irfan, A. Idris and N. M. Yusof, *J. Taiwan Inst. Chem. Eng.*, **47**, 50 (2015).
30. S. Samadi, S. M. H. Mirseyfifard, M. Assari and M. Hassannejad, *Water Sci. Technol.*, **76**, 15 (2017).
31. W. S. H. Jr and R. E. Offeman, *J. Am. Chem. Soc.*, **80**, 1339 (1958).
32. Y. Cao, M. Hassan, Y. Cheng, Z. R. Chen, M. Wang, X. Z. Zhang, Z. S. Haider and G. Zhao, *ACS Appl. Mater. Interfaces*, **11**, 12379 (2019).
33. D. L. Zhao, X. Gao, C. N. Wu, R. Xie, S. J. Feng and C. L. Chen, *Appl. Surf. Sci.*, **384**, 1 (2016).
34. D. Dupont, W. Brullot, M. Bloemen, T. Verbiest and K. Binnemans, *ACS Appl. Mater. Interfaces*, **6**, 4980 (2014).
35. M. R. Farani, P. Khadiv-Parsi, G. H. Riazi, M. S. Ardestani and H. S. Rad, *Appl. Nanosci.*, **10**, 1205 (2020).
36. D. Yamini, G. D. Venkatasubbu, J. Kumar and V. Ramakrishnan, *Spectrochim. Acta. Part A.*, **117**, 299 (2014).
37. M. M. Bidhendi, G. Garcia-Olvera, B. Morin, J. S. Oakey and V. Alvarado, *SPE J.*, **23**, 803 (2018).
38. J. A. Ali, K, Kolo, A. K. Manshad and K. D. Stephen, *Energy Fuels*, **33**, 927 (2019).
39. A. Sony, H. Suhaimi and L. C. Rose, *Orient. J. Chem.*, **35**, 571 (2019).
40. H. Yan, S. L. Yuan, G. Y. Xu and C. B. Liu, *Langmuir*, **26**, 10448 (2010).
41. X. Y. Jin, M. Q. Jiang, J. H. Du and Z. L. Chen, *J. Ind. Eng. Chem.*, **20**, 3025 (2014).
42. S. Mopoung and T. Bunterm, *Carbon: Sci. Technol.*, **8**, 13 (2016).
43. J. H. Chen, H. T. Xing, H. X. Guo, W. Weng, S. R. Hu, S. X. Li, Y. H. Huang, X. Sun and Z. B. Su, *J. Mater. Chem. A.*, **2**, 12561 (2014).
44. N. You, Y. X. Song, H. R. Wang, L. X. Kang, H. T. Fan and H. Yao, *J. Chem. Eng. Data.*, **64**, 1378 (2019).
45. J. T. Sun, Z. P. Zhang, J. Ji, M. L. Dou and M. L. F. Wang, *Appl. Surf. Sci.*, **405**, 372 (2017).
46. L. Zhang, L. Zheng, J. Pu, C. Pu and S. Cui, *Energy Fuel*, **30**, 9351 (2016).
47. R. Liu, D. J. Du, W. F. Pu, J. Zhang and X. B. Fang, *Energy Fuels*, **32**, 12128 (2018).
48. W. F. Pu, J. Y. Gu, T. H. Zhao, L. Liu, N. Wang and F. Gu, *J. Surfactants Deterg.*, **20**, 1037 (2017).

Supporting Information

A novel recyclable nano-adsorbent for enhanced oil recovery with efficient removal of Ca^{2+} and Cr^{6+} from oilfield wastewater

Lei He*,‡, Yong Dai*,‡, Zhe Wang, Lutao Yang*, Luxia Zhang*, Pengpeng Hu*, Yu Tian*, Hong Mo*, Haomiao Zhu*,†, and Jun Zhang*,†**

*Jiangsu Collaborative Innovation Center of Biomedical Functional Materials, National and Local Joint Engineering Research Center of Biomedical Functional Materials, Jiangsu Engineering Research Center of Biomedical Function Materials, School of Chemistry and Materials Science, Nanjing Normal University, Nanjing 210023, China
**Key Laboratory of Oilfield Chemistry, Research Institute of Petroleum Exploration and Development (RIPED), CNPC, Beijing 100083, China
(*Received 25 March 2021 • Revised 18 January 2022 • Accepted 20 February 2022*)

1. Standard Curve

Table S1. Cr^{6+} standard working concentration and absorbance

Cr^{6+} concentration/mg·L^{-1} (X)	0.2	0.4	0.6	0.8	1.0
Absorbance (Y)	0.06474	0.13548	0.20584	0.27637	0.34893

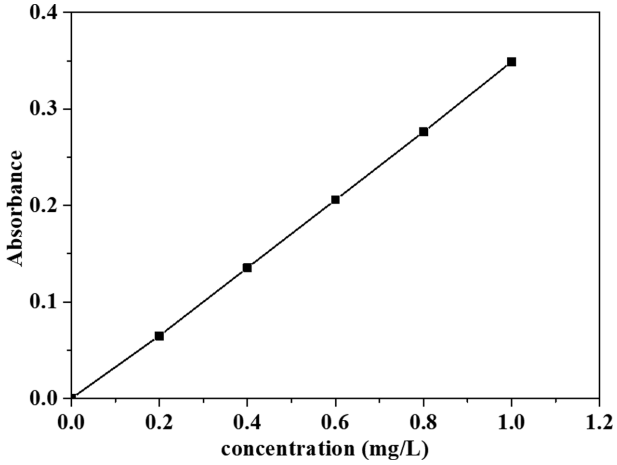


Fig. S1. Cr^{6+} standard working concentration and absorbance.

Trendline formula: Y=0.3546X−0.0065

$$R=\frac{E\{[X-E(X)][Y-E(Y)]\}}{\sqrt{D(X)D(Y)}} \quad R^2=0.999$$

2. Atomic Force Microscope (AFM)

Each sample (0.5 g) was dispersed in deionized water (150 mL) by ultrasonic waves for 20 min to obtain dispersion. The dispersion is dispersed on a mica plate. The morphology of the sample was observed with Bruker dimension edge AFM (Germany).

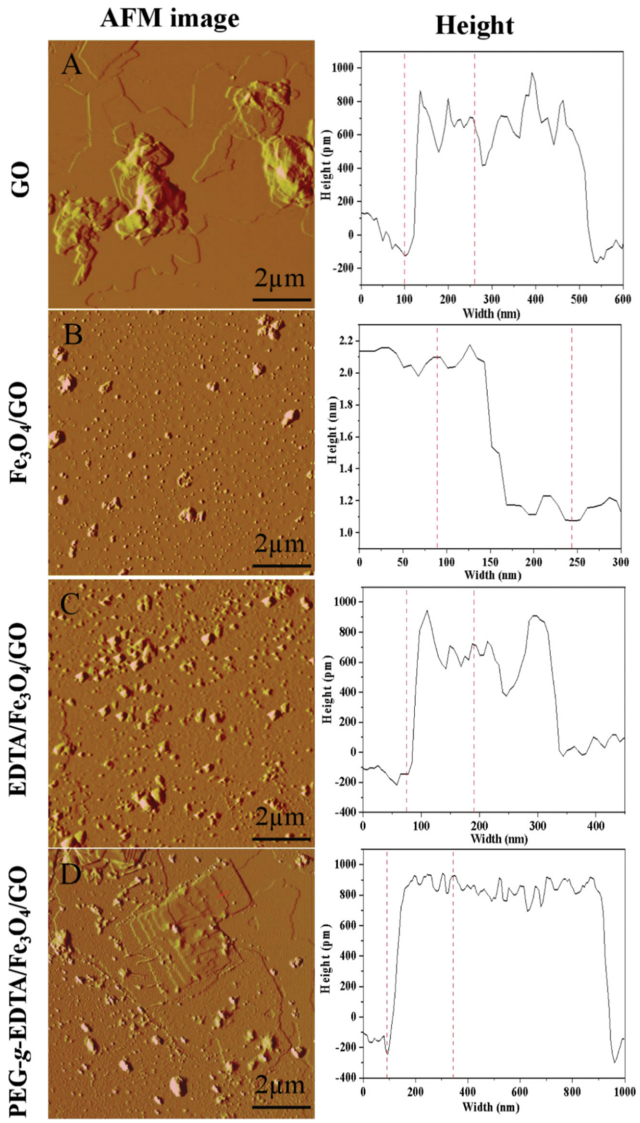


Fig. S2. AFM diagrams of GO (A), Fe_3O_4/GO (B), EDTA/Fe_3O_4/GO (C) and PEG-*g*-EDTA/Fe_3O_4/GO (D).

3. Scanning Electron Microscope (SEM)

Put the powders of GO, Fe_3O_4/GO, EDTA/Fe_3O_4/GO and PEG-*g*-EDTA/Fe_3O_4/GO samples respectively adhering to the conducting resin. Stick the conducting resin to the copper platform, and sparge copper on each face for three times. Use JSM-7600F (Japan) scanning electron microscope for testing.

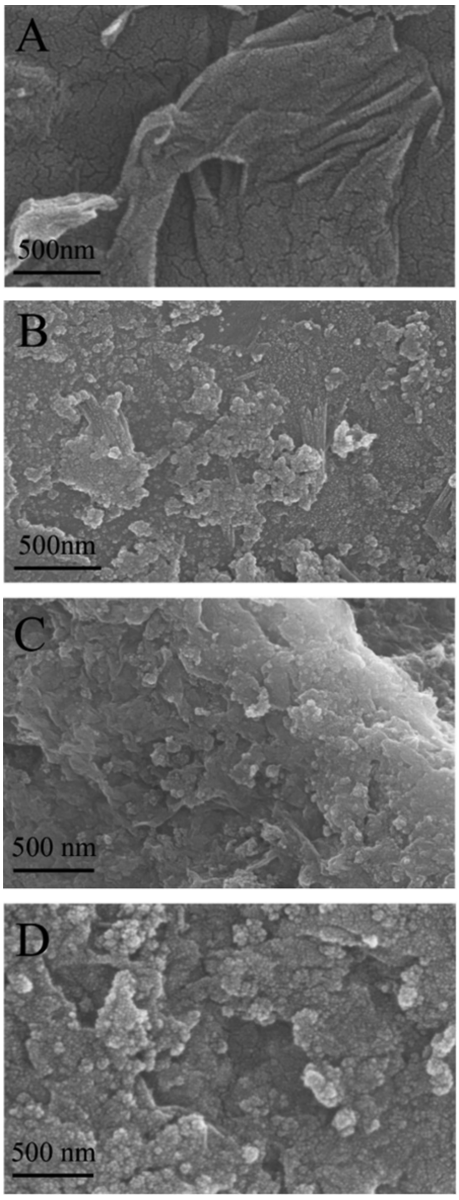


Fig. S3. SEM images of GO (A), Fe_3O_4/GO (B), EDTA/Fe_3O_4/GO (C) and PEG-*g*-EDTA/Fe_3O_4/GO (D).

4. Fourier Transform Infrared Spectroscopy (FT-IR)

Each sample was tested with the Nexus 670 FT-IR (USA). Scanning range: 4,000-400 cm^{-1}. FT-IR (KBr, cm^{-1}), GO: 3,700-3,000 (s, $v_{-OH-H2O}$), 1,734 (s, $v_{-C=O}$), 1,642 (s, $v_{-C=C-}$), 1,429 (s, β_{C-OH}), 1,049 (s, $v_{-C-O-C-}$). Fe_3O_4/GO: 3,700-3,000 (s, $v_{-OH-H2O}$), 588 (s, v_{Fe-O-}), 1,429 (s, β_{C-OH}), 1,049 (s, $v_{-C-O-C-}$). EDTA/Fe_3O_4/GO: 3,700-3,000 (s, $v_{-OH-H2O}$), 1,633 (s, $v_{-C=O}$), 1,401 (s, v_{-C-N}), 1,053 (s, $v_{-C-O-C-}$), 588 (s, v_{Fe-O-}). PEG-g-EDTA/Fe_3O_4/GO: 3,700-3,000 (s, $v_{-OH-H2O}$), 2,925 (d, v_{-CH2-}), 1,734 (s, $v_{-C=O}$), 1,209 (s, v_{-O-}), 588 (s, v_{Fe-O-}).

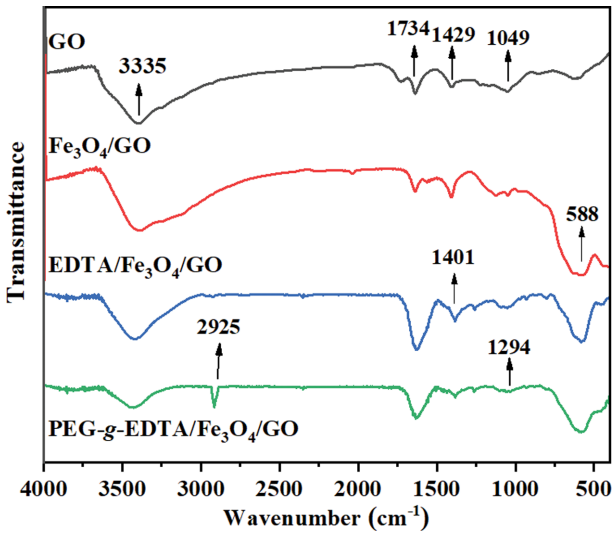


Fig. S4. FT-IR spectra of GO, Fe_3O_4/GO, EDTA/Fe_3O_4/GO and PEG-*g*-EDTA/Fe_3O_4/GO.

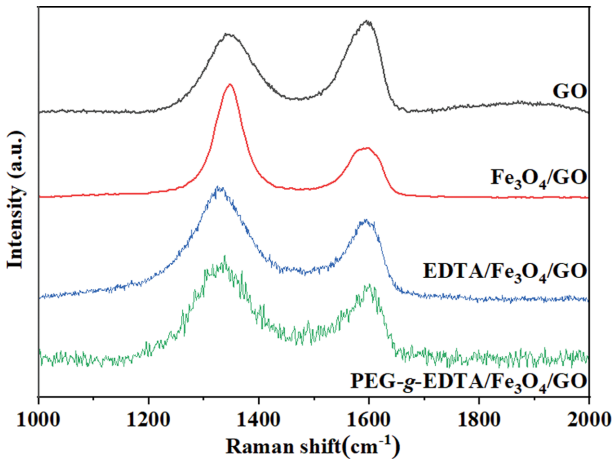


Fig. S5. Raman diagrams of GO, Fe_3O_4/GO, EDTA/Fe_3O_4/GO and PEG-*g*-EDTA/Fe_3O_4/GO.

5. Raman Spectra

Each sample was tested with LabRam HR Evolutionary Raman Spectrometer (Japan). The excitation wavelength is 633 nm, and the scanning range is 1,000-2,000 cm^{-1}.

6. XPS

7. Adsorption Test

Fig. S7 shows the adsorption capacity of Ca^{2+} and Cr^{6+} in simulated oilfield wastewater (Jidong Oilfield) by PEG-*g*-EDTA/Fe_3O_4/GO at different masses and at different times. The adsorption capacity of Both Ca^{2+} (a) and Cr^{6+} (b) increased with the increase of the mass of PEG-*g*-EDTA/Fe_3O_4/GO. The adsorption capacity of Ca^{2+} decreased and trended to be fiat after 0.4 g, and the adsorption

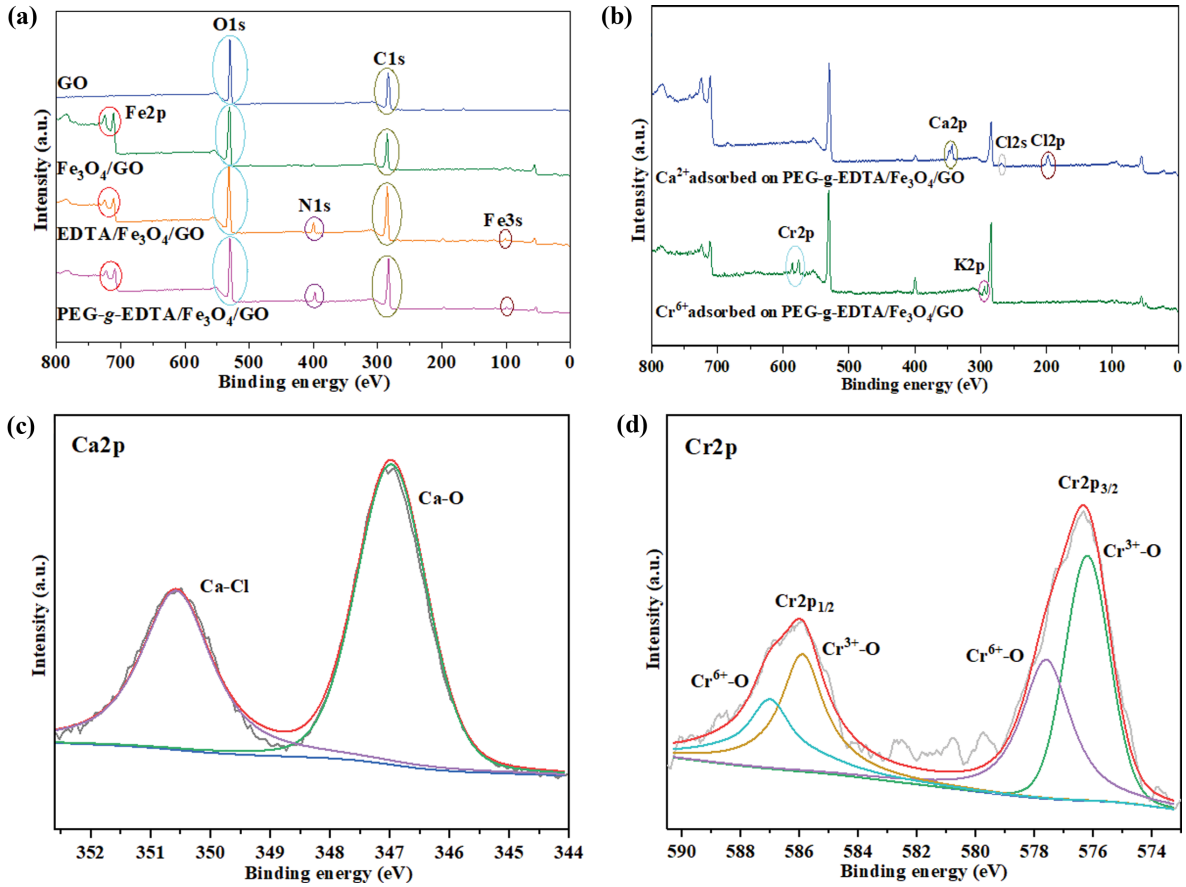


Fig. S6. XPS spectra: (a) wide scan, (b) wide scan of Ca^{2+} and Mg^{2+} adsorbed on PEG-*g*-EDTA/Fe_3O_4/GO, (C) Ca 2p of Ca^{2+} adsorbed on PEG-*g*-EDTA/Fe_3O_4/GO, (D) Cr 2p of Cr^{6+} adsorbed on PEG-*g*-EDTA/Fe_3O_4/GO.

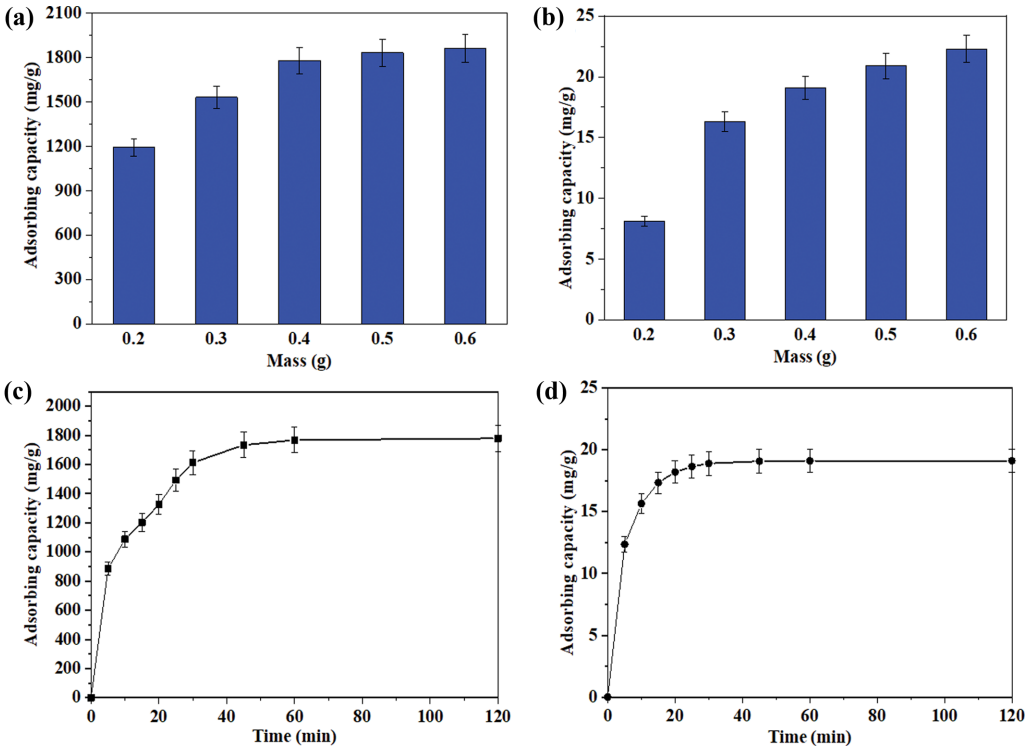


Fig. S7. Adsorption capacity of Ca^{2+} (a) and Cr^{6+} (b) by PEG-*g*-EDTA/Fe_3O_4/GO of different mass; at different time, 0.4 g PEG-*g*-EDTA/Fe_3O_4/GO to Ca^{2+} (c) and Cr^{6+} (d) adsorption capacity.

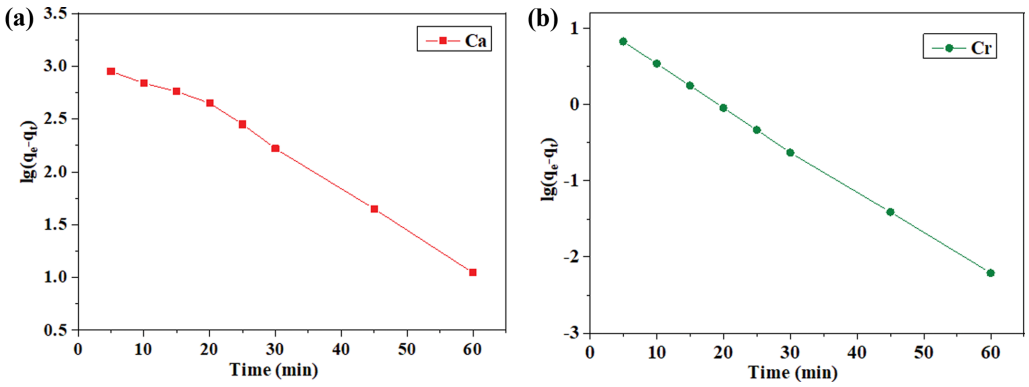


Fig. S8. Quasi-first-order kinetics simulation of PEG-*g*-EDTA/Fe_3O_4/GO adsorption for Ca^{2+} (a) and Cr^{6+} (b).

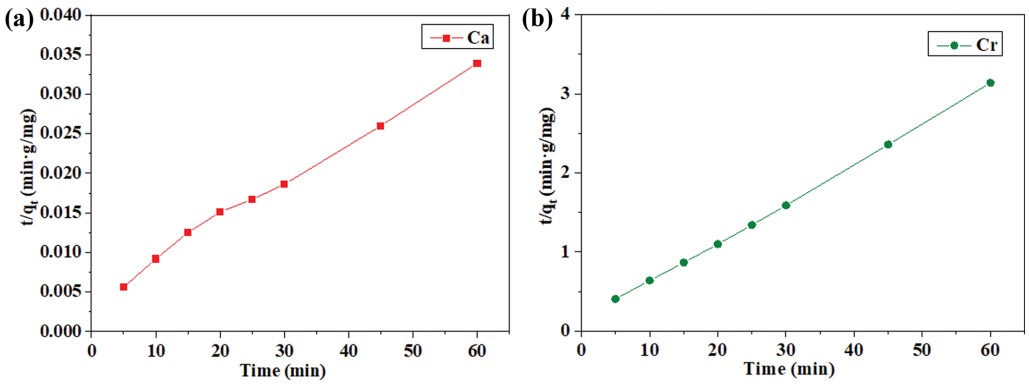


Fig. S9. Quasi-second-order kinetics simulation of PEG-*g*-EDTA/Fe_3O_4/GO adsorption for Ca^{2+} (a) and Cr^{6+} (b).

Table S2. Adsorption kinetic constants

Ion	$q_{e,exp}$ (mg/g)	Quasi-first-order			Quasi-second-order		
		$q_{e,cal}$ (mg/g)	k_1 (min^{-1})	R^2	$q_{e,cal}$ (mg/g)	k_2 (min^{-1})	R^2
Ca^{2+}	1,779	3,498	0.0356	0.95	2,000	0.0005	0.99
Cr^{6+}	19.12	30.99	0.0553	0.97	20.08	0.0498	0.99

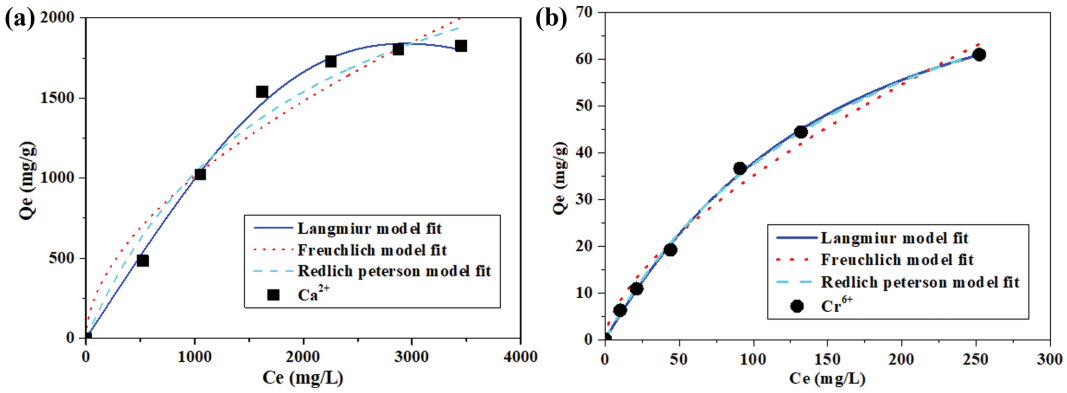


Fig. S10. Adsorption isotherm of PEG-*g*-EDTA/Fe_3O_4/GO adsorption for Ca^{2+} (a) and Cr^{6+} (b).

capacity of Cr^{6+} leveled off after 0.5 g. However, considering the adsorption effect and cost, we used 0.4 g PEG-*g*-EDTA/Fe_3O_4/GO for the adsorption experiment. The adsorption capacity of Ca^{2+} (c) and Cr^{6+} (d) increased sharply within 5 min. At 5 min, 10 min, and 30 min, the adsorption capacity of Ca^{2+} was 886, 1,087, and 1,613 mg/g, respectively. Subsequently, with the extension of adsorption time, the adsorption capacity of Ca^{2+} increased slightly. At 5, 10 and 30 minutes, the adsorption capacity of Cr^{6+} is 12.36, 15.65 and 18.89 mg/g, respectively. After that, with the extension of the adsorption time, the adsorption amount of Cr^{6+} did not increase significantly.

8. Kinetics Simulation

Fig. S8 shows the Quasi-first-order kinetics simulation of PEG-*g*-EDTA/Fe_3O_4/GO adsorbing Ca^{2+} and Cr^{6+}. Quasi-first-order kinetics was obtained by plotting the curves on adsorption time t and $lg(q_{e,exp}-q_t)$ in which $q_{e,exp}$ represented the maximal adsorption capacity at adsorption time t. As to Ca^{2+}, the curve was fitted to the equation y=−0.0356x+3.2352, with a maximal theoretical adsorption capacity $q_{e,cal}$ of 3,498 mg/g. As to Cr^{6+}, the curve was fitted to the equation y=−0.0553x+1.0745, with a theoretical adsorption capacity $q_{e,cal}$ of 30.99 mg/g.

Fig. S9 shows the Quasi-second-order kinetics simulation of PEG-*g*-EDTA/Fe_3O_4/GO adsorbing Ca^{2+} and Cr^{6+}. The Quasi-second-order kinetics was obtained by plotting the correlation curve of t and t/q_t. As to Ca^{2+}, the curve was fitted to the equation y= 0.0005x+0.0043, with a maximal theoretical adsorption capacity $q_{e,cal}$ of 2,000 mg/g. As to Cr^{6+}, the curve was fitted to the equation y=0.0498x+0.1223, with a theoretical adsorption capacity $q_{e,cal}$ of 20.08 mg/g.

Since the variance R^2 of quasi-second-order kinetics simulation was nearer to 1 relative to that of quasi-first-order kinetics simulation, it was considered that the adsorption mechanism of PEG-*g*-EDTA/Fe_3O_4/GO to Ca^{2+} and Cr^{6+} met quasi-second-order kinetics.

9. Adsorption Isotherm

Fig. S10 demonstrates the isotherm equilibrium data as points obtained on the adsorption of Ca^{2+} and Cr^{6+} by PEG-g-EDTA/Fe_3O_4/GO. To evaluate the nature of the adsorption reaction, the data was analyzed with the non-linear fit methods shown below:

Langmuir model:

$$Q_e = Q \times K \times C_e / (1 + K \times C_e) \quad \text{(S1)}$$

Freundlich model:

$$Q_e = K_f \times C_e^{(1/n)} \quad \text{(S2)}$$

In formula S1 and 2 Q_e has usual significance, Q the monolayer adsorption capacity (mg/g), C_e is the equilibrium solute concentration (mg/L), K, K_f are the Langmuir and Freundlich isotherm constants, respectively.

Table S2. shows that the R^2 of Langmuir model is closer to 1 than that of Freundlich, so it can be judged that it is mainly monolayer adsorption.

10. Emulsification Test Results

Fig. S11(a) is the height of the emulsified layer measured by the displacement fluid prepared by untreated oilfield wastewater, and Fig. S11(b) is the height of the emulsified layer measured by the displacement fluid prepared by PEG-*g*-EDTA/Fe_3O_4/GO treated

Table S3. Adsorption isotherm constant

Adsorption model		Ca^{2+}	Cr^{6+}
Langmuir	Q (mg/g)	2,580.99	104.83
	K (L/mg)	6.71×10^{-4}	5.57×10^{-3}
	R^2	0.976	0.998
Freundlich	K_f (mg/g)	22.46	1.87
	n	0.81	1.57
	R^2	0.952	0.988

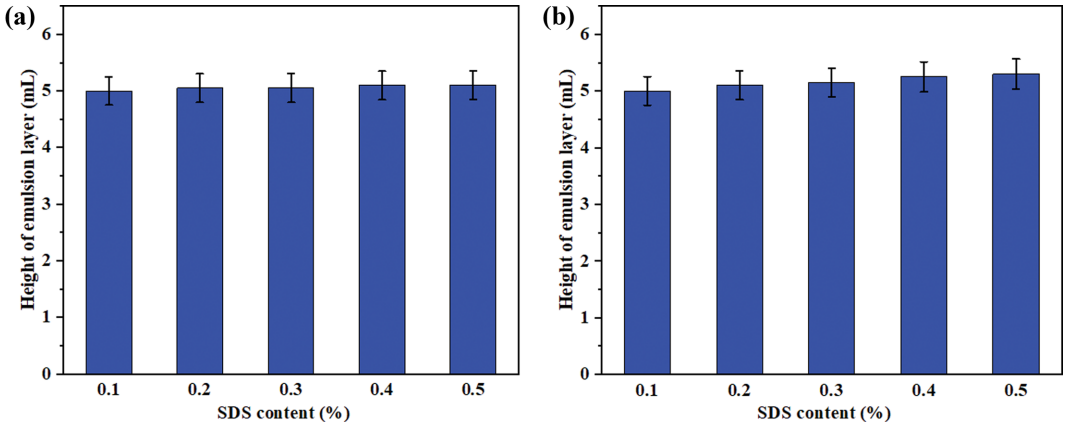


Fig. S11. Emulsification performance test of displacement fluid prepared by oilfield wastewater before (a) and after (b) treatment with PEG-*g*-EDTA/Fe_3O_4/GO.

oilfield wastewater. The above results indicated that the emulsification performance of SDS displacement solution treated by PEG-*g*-EDTA/Fe_3O_4/GO could be improved to some extent. This is because after treatment, the salt content in oilfield wastewater decreases, so the emulsification increases.

11. Calculation of Interfacial Tension

Calculate the interfacial tension using the following equation when the length (L) and diameter (D) ratio L/D of one oil drop was >4:

$$\gamma = \frac{\Delta\rho \times \omega^2 \times Y^3}{4} \quad \text{(S3)}$$

In formula S3, γ: interfacial tension (mN/m) of the oilfield water; $\Delta\rho$: the density gradient between two liquid phases (g/cm^3); ω: angular velocity (rad/s); Y: the maximal vertical radius (cm) of one oil drop after being extended.

Calculate the interfacial tension using the following equation when the length (L) and diameter (D) ratio L/D of one oil drop was <4:

$$\gamma = \frac{\Delta\rho \times \omega^2 \times R^3}{4 \times \left(\frac{x}{b} - 1\right)} \quad \text{(S4)}$$

In formula S4, γ: the interfacial tension (mN/m) of the oilfield water; $\Delta\rho$: the density gradient between two liquid phases (g/cm^3); ω: angular velocity (rad/s); X: the half length of one oil drop (cm); b: the radius of curvature on the top of one oil drop; *R*: the radius of curvature (cm).

$$R = \left(\frac{3V}{4\pi}\right)^{1/3} \quad \text{(S5)}$$

In formula S5, R: the radius of curvature (cm); V: the sphere volume with R as the radius (cm^3).

12. Core Data Calculate of Simulated Indoor Oil Recovery Test

The pore volume (V_r) of the Berea core can be calculated as follows.

$$V_r = \frac{W_w - W_d}{\rho_w} \quad \text{(S6)}$$

where W_w and W_d are the wet weight and the dry weight of the Berea core, respectively. ρ_w is the density of reinjection water.

The initial oil saturation (C_p) of the Berea core can be calculated as follows.

$$C_p = \frac{V_p}{V} \times 100\% \quad \text{(S7)}$$

Where V_w is the volume of water displaced by the saturated oil. The water phase permeability (K_w) can be calculated as follows.

$$K_w = \frac{Q \times \mu_w \times L}{A \times \Delta P} \times 1{,}000 \quad \text{(S8)}$$

where Q is the flow quantity of the displacing phase, μ_w is the viscosity of the water phase, L is the length of the Berea core, A is the sectional area of the Berea core, ΔP is the differential pressure between the two ends of the Berea core during injecting.

The real-time oil recovery efficiency (C_r) in the core displacing experiments can be calculated as follows.

$$C_r = \frac{V_o}{V_p \times C_o} \times 100\% \quad \text{(S9)}$$

where V_o is the accumulated volume of the displaced oil, V_p is the pore volume of the Berea core.

13. Displacement Experiment Procedure

Step 1: The Berea core parameters were measured (including length, diameter, dry weight, etc.), followed by the vacuum process. Later, the core saturated water test was performed for 24 h to measure the core wet weight and pore volume. Then, the core was put into the holder of the displacement device to measure the core aqueous phase permeability (Tables S3 and S4).

Step 2: The target oil reservoir was injected into the core to dehydrate the crude oil. Then, the aqueous phase in the core was replaced until no water efflux occurred and was aged for 48 h at the target oil reservoir temperature (60 °C).

Step 3: Simulated water was used as the displacement phase to displace the crude oil in the core until the water content was >98%, and the displacement was stopped after 0.5 PV was stable.

Step 4: Untreated reinjection water was used to prepare 0.3% SDS for displacement (Fe_3O_4/GO-COOH-treated reinjection water was used to prepare displacement fluid containing 0.3% SDS in the

Table S4. The length, the diameter, the Cross-sectional area, the dry weight and the wet weight of the Berea core

Lenth (cm)	Diameter (cm)	Cross-sectional area (cm^2)	Dry weight (g)	Wet weight (g)
20.0	3.80	11.34	460.8	513.4

Table S5. The pore volume, the porosity, the aqueous permeability and the oil saturation of the Berea core

Pore volume (cm^3)	Porosity (%)	Aqueous permeability (10^{-3} μm^2)	Oil saturation (%)
52.6	23.2	30.1	62.4

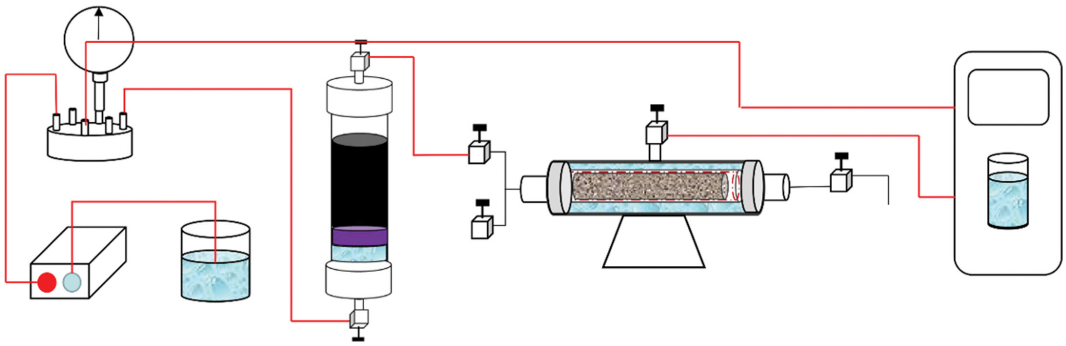


Fig. S12. Schematic diagram of a displacement device.

second displacement process) until the water content was >98% and stabilized at 0.5 PV.

Step 5: Simulated water was used as the chemical agent after water flooding. The displacement test ended when there was no oil efflux. The displacement device chart is shown in Fig. S11.